

# PROCEEDINGS OF SPIE

[SPIDigitalLibrary.org/conference-proceedings-of-spie](https://spiedigitallibrary.org/conference-proceedings-of-spie)

## Full optical model of micro-endoscope with optical coherence microscopy, multiphoton microscopy and visible capabilities

David Vega, Kelli C. Kiekens, Nikolas C. Syson, Gabriella Romano, Tressa Baker, et al.

David Vega, Kelli C. Kiekens, Nikolas C. Syson, Gabriella Romano, Tressa Baker, Jennifer K. Barton, "Full optical model of micro-endoscope with optical coherence microscopy, multiphoton microscopy and visible capabilities," Proc. SPIE 10470, Endoscopic Microscopy XIII, 104700M (14 February 2018); doi: 10.1117/12.2285059

**SPIE.**

Event: SPIE BiOS, 2018, San Francisco, California, United States

# Full optical model of micro-endoscope with optical coherence microscopy, multiphoton microscopy and visible capabilities

David Vega<sup>\*a</sup>, Kelli C. Kiekens<sup>a</sup>, Nikolas C. Syson<sup>a</sup>, Gabriella Romano<sup>b</sup>, Tressa Baker<sup>c</sup>, Jennifer K. Barton<sup>a,b</sup>

<sup>a</sup>College of Optical Sciences, The University of Arizona, AZ, 85721; <sup>b</sup>Biomedical Engineering, The University of Arizona, AZ, 85721; <sup>c</sup>Catalina Foothills High School, Tucson, AZ, 85719.

## ABSTRACT

While Optical Coherence Microscopy (OCM), Multiphoton Microscopy (MPM), and narrowband imaging are powerful imaging techniques that can be used to detect cancer, each imaging technique has limitations when used by itself. Combining them into an endoscope to work in synergy can help achieve high sensitivity and specificity for diagnosis at the point of care. Such complex endoscopes have an elevated risk of failure, and performing proper modelling ensures functionality and minimizes risk. We present full 2D and 3D models of a multimodality optical micro-endoscope to provide real-time detection of carcinomas, called a salpingoscope. The models evaluate the endoscope illumination and light collection capabilities of various modalities. The design features two optical paths with different numerical apertures (NA) through a single lens system with a scanning optical fiber. The dual path is achieved using dichroic coatings embedded in a triplet. A high NA optical path is designed to perform OCM and MPM while a low NA optical path is designed for the visible spectrum to navigate the endoscope to areas of interest and narrowband imaging. Different tests such as the reflectance profile of homogeneous epithelial tissue were performed to adjust the models properly. Light collection models for the different modalities were created and tested for efficiency. While it is challenging to evaluate the efficiency of multimodality endoscopes, the models ensure that the system is design for the expected light collection levels to provide detectable signal to work for the intended imaging.

**Keywords:** micro-endoscope, optical design, OCT, OCM, MPM, multimodal endoscopy.

## 1. INTRODUCTION

It is estimated that ovarian cancer (OC) accounted for more than 22,000 new diagnoses of cancer among women in 2017, and it causes more deaths than any other cancer of the female reproductive system accounting for more than 14,000 deaths per year<sup>1</sup>. The statistics for 2017 suggest OC has very low survival rate being the fifth deadliest cancer among women principally due to late diagnosis. Proper diagnosis is prevented due to the lack of techniques to diagnose it at early stages, the lack of symptoms, and the desire to reduce the very invasive procedures of laparoscopy to try to detect OC. There has been limited success in developing a screening method for OC, motivating our innovative method to detect early stages of OC. A successful early detection technique can improve the survival rate of affected women since stage 1 is 90%, whereas the rate at stage 3 is only 38%, with its lowest at stage 4 of 17%<sup>1</sup>.

### 1.1 OCM and MPM for cancer detection

As with many other cancers, the gold standard for OC is histology of the tissue. Unfortunately, this method is invasive due to the need to obtain a tissue sample. Additionally, preparation of the sample is time consuming, sampling error may occur, and staining of the sample is required to achieve high contrast. Histology of the tissue may take days or weeks and requires a lab setting. Alternatively, there are different techniques that can be used to identify carcinomas in vivo. The techniques that we focus on are OCM and MPM. These techniques can work in synergy to achieve high specificity and sensitivity<sup>2</sup> for diagnosis at the point of care. These two systems when combined take the advantage of the high contrast, high resolution imaging of MPM without the need for any contrast agents for surface microscopy of tissue, and the high spatial resolution of OCM for morphology information of the tissue. However, the combination of the two separate methods MPM and OCM may add complexity, size and cost. Additionally, narrowband imaging has been used clinically to detect cancer<sup>15,16</sup>, and is useful as a lower resolution, larger field of view navigation technique to identify areas of interest for high resolution imaging.

\*dvega@optics.arizona.edu;

phone:1-520-626-4463;

<http://bmeoptics.engr.arizona.edu>

## 1.2 Previous Designs

Our design was first inspired by a dual modality 3 mm diameter microendoscope presented by Dimitre Ouzounov<sup>3</sup>. This design shows a 9x optical zoom capability that requires no mechanical adjustment of the distal elements. The zoom is accomplished by separating the optical path of different wavelengths used in different magnifications. Multilayered dichroic surfaces are used to create these different optical paths. This design features multiphoton fluorescence imaging and one photon reflectance imaging. This unique device allowed forward viewing for navigation and imaging; a modality often requested by physicians for endoscopic imaging. While Ouzounov's design is unique and novel, we were unable to fully adapt it to our needs.

Instead we looked at adapting a Cassegrain telescope like structure to be used as a beam expander combined with a previous design (falloscope<sup>4</sup>) from our lab, to obtain our optical system, as explained in the design section below. The falloscope features a ~65 degrees Full Field of View (FFOV) that is designed for visible navigation and fluorescent imaging. While our system does not use the fluorescent imaging and it has a slightly lower FFOV, the system utilizes the same principle of lens stacking for the optical system for a compact optical system that is easier to align and build.

An important part of our design is the laser utilized. While Ti-Sapphire laser is commonly used for MPM, it is bulky and expensive. Additionally, the laser used should be capable of performing MPM and OCM using the same optical system. It was previously demonstrated that OCM and MPM can be performed using a compact ultrafast femtosecond fiber-based supercontinuum source<sup>5,6</sup>. Using such supercontinuum sources is much more effective both in space and price, but presents a challenge to the dichroic coatings since the bands that should be reflected and transmitted are wider.

## 1.3 Paper Overview

The analysis methods are presented in Section 2 below. Section 2.1 describes OCM, MPM and design requirements that were taken in consideration, in order to provide the reader an example of how a multimodal endoscope can be initially idealized. Section 2.2 presents the final optical design and explains the method used to arrive at this optical system. Also, a brief discussion about the dichroic surfaces in this endoscope is included and the incorporated illumination and collection systems are described. Section 2.3 identifies how models provide the ability to identify potential failures and address concerns. Section 2.4 explains in detail how the models were or were not customized to accommodate for the different modalities. This section also explains an experiment performed to obtain a reflection profile for epithelial tissue. Finally, the section includes the assumptions made in the models to decrease the complexity of model customization. In section three, significant results are presented, including design tradeoffs, results from the sequential ray trace models, and results from the non-sequential ray trace models. We conclude with the current status of this project and future plans, and the implications of results obtained by the models.

# 2. METHODS

## 2.1 Design Requirements

As explained by Fujimoto et al<sup>7</sup>, in OCT the transverse resolution  $\Delta x$  is directly related to the spot size on the objective lens and the focal length of the objective.

$$\Delta x = \frac{4\lambda f}{\pi d} \approx \frac{2\lambda}{\pi(\text{NA}_o)} \quad (1)$$

where  $d$  is the spot diameter representing an exit pupil that is fully illuminated by a Gaussian beam,  $\lambda$  is the wavelength,  $f$  is the focal length and  $\text{NA}_o$  is the object space numerical aperture of the system in the paraxial approximation. Additionally, the transverse resolution is also related to the depth of focus (DOF) by the following relationship

$$\text{DOF} = \pm \frac{\pi(\Delta x)^2}{\lambda} \approx \pm \frac{4\lambda}{\pi(\text{NA}_o)^2} \quad (2)$$

Approximations for equations 1 and 2 are only valid in the paraxial limit and must be used with caution. Note that by increasing the  $\text{NA}_o$ , the DOF decreases and by increasing the wavelength, the DOF increases. Therefore, in a high  $\text{NA}_o$  system, the DOF can be increased by the use of larger wavelengths.

In MPM, it has been shown that the amount of fluorescence generated from a given axial plane decreases in a quadratic fashion away from the focal plane<sup>8</sup>. Therefore, the integrated excitation of fluorophores is a function of the axial distance

z, but only light with  $z \leq \text{DOF}$  contributes significantly to the signal. Transverse resolution  $\Delta x$  for MPM follows the following relationship<sup>8</sup>:

$$\Delta x = .6 \frac{\lambda}{(\text{NA}_o)} \quad (3)$$

This equation almost matches the paraxial approximation in equation 1. This allows us to choose an  $\text{NA}_o$  where OCM and MPM have similar transverse resolution. It is usually preferred to choose a low  $\text{NA}_o$  for Optical Coherence Tomography (OCT) to increase the DOF and obtain signal deeper in the tissue. While in an application where functional imaging (provided by MPM) and morphological imaging (provided by OCM) are desired of the same volumetric tissue, a larger  $\text{NA}_o$  may be preferred by sacrificing the DOF for OCT but instead obtaining OCM. In this way, the instrument can achieve approximately the same resolution for both functional and morphological maps of the volumetric tissue. The FOV for OCM and MPM should ideally be larger than 100  $\mu\text{m}$  to image a representative sampling of tissue.

A desired lateral resolution for OCM and MPM to achieve subcellular imaging is about 2  $\mu\text{m}$ . By using a laser of wavelength  $\lambda=1300 \text{ nm}$  and following the equations 1 and 3 to solve for the required  $\text{NA}_o$ , this resolution can be achieved with an  $\text{NA}_o \approx .40$ . For the navigation system, a lower  $\text{NA}_o$  should be available to have long DOF, large FFOV to navigate the endoscope. Initially, we targeted a navigation  $\text{NA}_o$  of about .012 and 3 mm working distance similar to the specification of the falloposcope. Also, note that the FFOV for the visible navigation channel was left unconstrained to have some flexibility, but 70° degrees was desirable.

Table 1. Initial desired optical system specifications.

Specification	Value
High NA (HNA)	.40
HNA full field of view	100 $\mu\text{m}$
HNA scanning	Quartered piezo tube scanning
HNA working distance	.50 $\mu\text{m}$ (for contact scanning)
Low NA (LNA)	.012
LNA full field of view	70° (desirable)
LNA scanning	Quartered piezo tube scanning
LNA working distance	Unconstrained
Diameter	1.5 mm
Illumination fiber NA	.12

In our application for imaging the ovaries, it was desired that the endoscope be flexible, and be introduced through the vagina wall to reach the ovaries and fallopian tubes. This restriction limited the longitudinal size of the optical system since a short rigid ferrule is desired. Also, the endoscope diameter is an important parameter. In this project, the total diameter of the endoscope was constrained to an already accepted standard, egg harvesting needles for in vitro fertilization (IVF) tools, which are approximately 3 mm in diameter. Therefore, we limited our endoscope to 3.5 mm, for an endoscope which includes a biopsy channel, an irrigation channel, and the optical system. Our biopsy mechanism has a diameter of 1.34 mm, and the irrigation channel has a diameter of .97 mm, leaving only ~1.9 mm for the optical system. During the preliminary design phase, it was decided that the lenses would be 1.5 mm in diameter, and that the high resolution systems would work in contact with the tissue. It was additionally determined that a double-clad fiber (Thorlabs, DCF13) would be used for illumination and collection. This fiber has a core NA of .12. Furthermore, all modalities including OCM, MPM and the LNA navigation channel require a scanning system. A very effective scanning system for this kind of microendoscope is presented by Lee et al<sup>9</sup>. This system uses a quartered piezo tube (QPT) with a cantilevered fiber fixed to one end and the other end is fixed to an acrylic collar. By applying different voltage frequencies to the x and y axis of the QPT, different scanning patterns can be achieved. Table 1 presents a summary of the desired system specifications.

## 2.2 Optical Design, Embedded Dichroic Surfaces, and Optical Modalities.

The falloposcope was used as the starting point for this optical design. It was combined with a Cassegrain telescope like structure used as a beam expander to achieve the HNA. Initially the Cassegrain telescope was modeled with a lens to verify that this technique would work. Figure 1 shows this model in the collection mode.

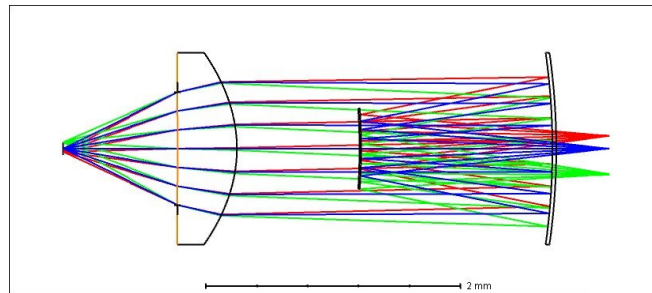


Figure 1. Cassegrain telescope combined with an aspheric objective designed to accomplish the HNA optical path.

In this diagram, the tissue is on the left and the source is on the right. This initial design ensured that the system would be able to collect an OCM signal with .40 NA into the dual clad fiber at .12 NA. After verifying this capability, the principle was applied to the falloposcope (Figure 2) to arrive to the current design of the salpingoscope.

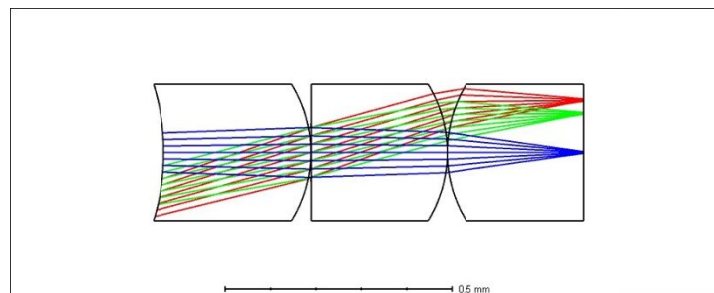


Figure 2. Falloposcope design, adapted from Tyler et al[3].

The telescope like structure is to be achieved with dichroic coatings such as in Ouzounov's design<sup>3</sup>. It was first attempted to place these dichroic surfaces in the back of the first element and the back of second element of the falloposcope, but current manufacturing capabilities do not allow this solution to be build due to the need of strong curvatures in very small diameters. Instead a second solution that kept the staking of the lenses as a method to assemble the optical system was developed. The resulting solution is depicted in Figure 3. This system incorporates a triplet lens that has embedded dichroic surfaces to generate the telescope like optical path, and a frontal aspheric objective that achieves the HNA for wavelengths that reflect in the dichroic coatings. This triplet also serves as a positive lens for wavelengths that are not reflected by the dichroic surfaces making the LNA visible navigation possible using the same optical system. Note that element 5 of the optical system is a cover plate, modeled as a plane parallel plate made of fused silica.

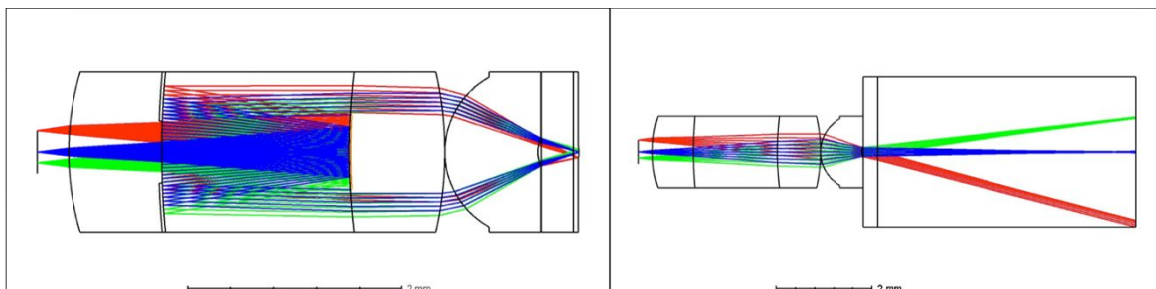


Figure 3. Left, HNA optical path for salpingoscope design featuring a triplet, and an objective. Right, LNA optical path. From left to right: First boundary is air and the object represents the fiber plane, Element 1 (S-LAH58), Element 2 (BK7), Element 3 (S-LAH79). Element 4 (ZnS broadband). Element 5 (Fused Silica).

The most novel structure of the optical system is the triplet, but specially the lens in the center or element 2. This lens features two dichroic surfaces and its depicted in Figure 4. The coatings were designed by Blue Ridge Optics (Bedford, VA) with a theoretical curve also shown in Figure 4.

As seen in the theoretical curve for the dichroic surfaces in figure 4, it allows the transmission of short wavelengths and the reflection of long wavelengths. This allows a spectrum centered around 1350 nm to achieve both OCM and MPM and any wavelength illumination between 450 to 850 nm to be transmitted for the navigation/narrowband system. Illumination at narrowband 520 nm was selected for the visible navigation system due to the availability in our lab and high absorption by hemoglobin increasing the contrast for the visible navigation system.

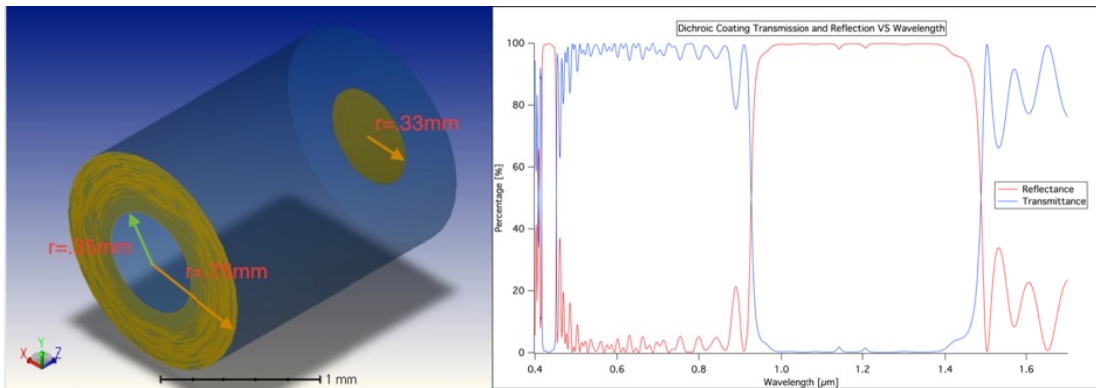


Figure 4. Left, 3D rendering of element 3-2 with dichroic coatings shown. Right, Dichroic coating theoretical curve at 0° light incidence.

Three light collection systems were incorporated to the optical system. Each modality has its own collection system based on the needs of the modality, and in some cases to avoid cross contamination of incoming signal. The OCM signal from tissue, is collected using the illumination fiber core, since this coherent light must travel through single mode fiber. The MPM second harmonic generation (SHG), two-photon excitation fluorescence (2PEF), third harmonic generation (THG), and three-photon excitation fluorescence (3PEF) are collected using the first cladding of the double-clad illumination fiber, which enables higher collection efficiency due to the large area and NA of the cladding. The visible reflections are collected by 12 multimode fibers (MMF) (Thorlabs-FP200URT) placed in the ferrule around the optical system with a large nominal NA of .50 depicted in Figure 5. Each collected signal will be processed in different parts of the proximal system presented by Kiekens et al<sup>10</sup>.

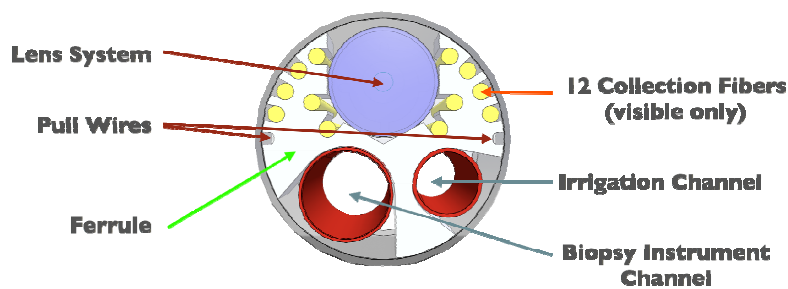


Figure 5. Front view of the salpingoscope.

Using the different illumination optical paths and the different collection systems, multiple modalities are accomplished. Figure 6 shows a summary of the different optical modalities and their related optical paths and wavelengths.





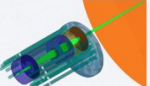
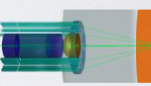
	Illumination	Illumination System		Collection	Collection System	
OCM	~1200 to 1400 nm	Fiber core, HNA		~1200 to 1400 nm	Fiber core, HNA	
MPM	~1200 to 1400 nm	Fiber core, HNA		~400 - 800 nm	Fiber cladding, LNA	
Visible	~520 nm	Fiber core, LNA		~520 nm	Collection fibers.	

Figure 6. Optical modalities with diagrams.

### 2.3 Methodology for sequential models

A main concern was to achieve both LNA and HNA optical paths in the same optical system using dichroic surfaces. The salpingoscope's unique constraints include small diameter and short rigid tip length. The ability to achieve a spot size near the diffraction limit is required by OCM and MPM, and this can be tested with a sequential model. The modulation transfer function was obtained to examine resolution.

An optimized sequential model implemented in Optic Studio from Zemax LLC was used to obtain the system information such as NA, spot size, and spatial frequencies. For some optical modalities, the optical system was used for both illumination and collection, therefore, the direction of light propagation was reversed. The illumination for all optical modalities was modeled by using the fiber as a source and the tissue as the "image" plane while the collection system for OCM was modeled from tissue to fiber, flipping the optical system in the ray trace software. The tissue plane was allowed to curve since a plane surface is not necessary for cancer detection. A sequential model for MPM collection and visible navigation systems was not possible due to scattering effects and dichroic surfaces.

### 2.4 Methodology for non-sequential models

A non-sequential model was built to interrogate the system for its efficiency collecting light, to assure that the system would have sufficient signal to noise ratio. Ouzounov<sup>3</sup> identified that the dichroic surfaces in their system prevented light from the 2PEF to be epi-collected. We determined our system's capability for collecting 2PEF, 3PEF, SHG, THG and OCM signal using this model.

To accurately test MPM and visible navigation, a 3D non-sequential customized model was created. The non-sequential model included the dichroic surface transmission and reflection profiles to accurately check performance at every wavelength used. The tissue reflectance profile was modeled using results from reflectance measurements performed with grocery store porcine tripe tissue (deemed suitably close to ovarian tissue). While most models treat tissue as a Lambertian reflector, that simplification may be inaccurate. As noted by Andersen et al<sup>11</sup> a reflectance profile, either specular, Gaussian, Lambertian or any other form, is affected by the Shower-Curtain effect and the profile depends on the observation plane. To ensure accuracy, a reflectance profile of the tissue was measured using a super luminescent diode laser output separated into two fiber arms using a coupler (Figure 7, Left). The tissue illumination arm and reference arm of the coupler were connected to collimators and directed toward their own power meter photodiodes for calibration. The calibration curve allowed the output power in the illumination to be known at any time by monitoring the reference arm. After obtaining this curve, the sample was mounted on a rotation stage and the illumination arm was placed above the sample and aligned to the sample axis of rotation (Figure 7, Right). A power meter photodiode was connected to a perpendicular rotation stage allowing 180° of movement centered on the sample. Radiance (M) was measured by rotation the photodiode from 0° to 180° to obtain a full profile around the sample. After obtaining a single profile, the sample was rotated 10° to obtain multiple reflectance profiles to average them and minimize errors in the final profile presented in Figure 8.

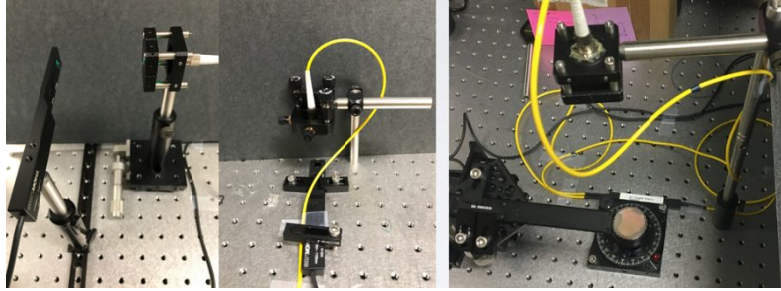


Figure 7. Left, illumination arm and reference arm respectively and photodiodes. Right, Sample and illumination arm with rotating photo diode. Note that the illumination arm shown in the left picture was rotated 90° to point downward to the sample

With this experiment, it was found that the reflectance profile is similar to the expected profile of a combination between Lambertian and specular reflectors affected by the shower-curtain effect. The lobes of the reflectance profiles are not purely Lambertian as often assumed in optical models, and the specular reflection is usually ignored. A single equation was not found to fit the final averaged profile; therefore, two Gaussian fits were applied, one along the lobes and another for the center peak (Figure 8). In our model, we used the integration of the two fit functions to calculate the fraction of reflected light and input the fraction in a Gaussian profile following basic radiometry calculations<sup>12</sup>. The model utilized reflects 6.5% of the total incoming light, where the it scatters 86.9% of the reflected light to the lobes distributed on a Gaussian profile with sigma set to .107 radians. The rest of the reflected energy goes to the specular reflection. Time constrains prevented us from using the perfect matched profile in non-sequential models. The only difference is that instead of a Gaussian function in the specular reflection, it reflects this energy in a delta function located at 0 radians.

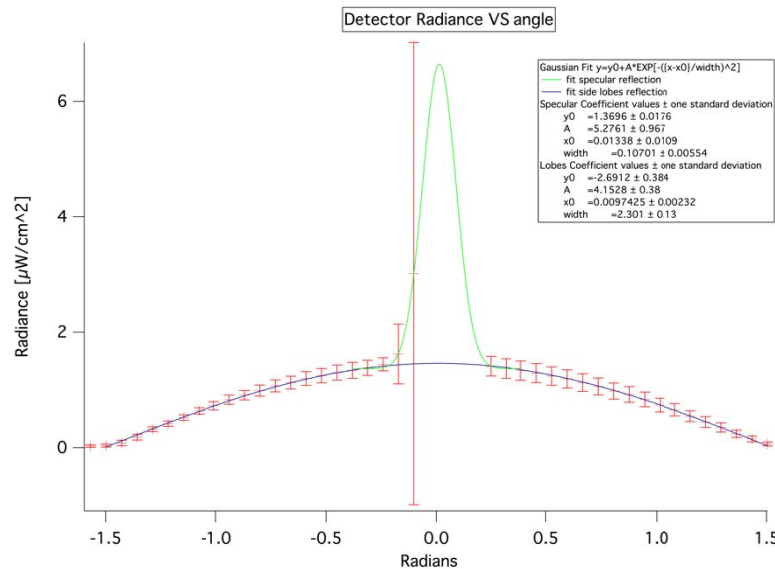


Figure 8. Radiance vs. angle of collection.

Another important customization was needed for the source of light needed. Optic Studio offers several different source options, but for the purpose of this optical system, the object type Source DLL is chosen to model a fiber source. In this object type, the fiber diameter is given by the parameter R and is set at 4.5 μm. The irradiance of the fiber is a function of distance from the fiber center,  $I(r) = A + B*r^2 + C*r^4$ , where A, B, and C are weight coefficients<sup>14</sup>. For simplicity, the model assumes that the fiber has a constant irradiance in the illumination profile, A is set to 1.00, and both B and C are set to 0.00. Finally, the NA of the fiber is given in Optic Studio<sup>14</sup> by  $NA(r) = D + E*r^2 + F*r^4$ . The nominal NA of the fiber used for illumination is 0.12, therefore D is set to 0.12, and E and F are set to 0.00. For the purpose of ray-tracing, the number of analysis rays is a primary concern, but convergence in results was observed using about 100,000 rays. Additionally, the source's power is set at 1.00W to normalize the efficiencies.

The collecting areas of the double-clad fiber are modeled using object type Detector Surface using circular shape for the OCM signal captured by the core, and an annulus shape for the MPM signal collected by the first cladding. The detectors were placed at the illumination fiber location with an offset of  $-.001 \mu\text{m}$  to the outgoing rays to allow for propagation of the source light forward without being absorbed by the detector. The Material for the detectors is set to ABSORB, to completely emulate the collection of all incident light. The resolution of the detector is defined by number of Angular Zones, and number of Radial Zones which are set to 208 and 175 respectively. The resolution is not necessarily a concern since the total light will be collected under high resolution or low; however, higher resolution allows a visual representation of where the light hits the sensor and is useful with off-axis simulations. To evaluate the illumination efficiencies of the HNA optical path, a Detector Surface was placed at the tissue distance of  $50 \mu\text{m}$ , the illumination fiber was set to illuminate with wavelengths starting at  $.9 \mu\text{m}$  to  $1.5 \mu\text{m}$  wavelength light, non-sequential ray trace was performed for each wavelength, and the collected power by the detector was obtained and normalized to obtain the efficiency. Similarly, for the collection efficiencies, the detectors from the double-clad fiber were used and a point source was placed at the tissue location to model either the reflected light for OCT or the emitted light for MPM signals.

The collecting areas of the MMF for the visible navigation system are modeled in the same way, but the detectors were placed inside fused silica cylinders to model the fibers. Unfortunately, Optic Studio does not have the capability to model fiber propagation. Therefore, the fused silica cylinders were set to be reflective in the side surfaces to allow the ray to propagate inside the volume. The drawback of using this technique is that the fiber NA is not modeled correctly, and the cylinder will propagate rays that hit the front surface at higher angles. This was not a concern in our model since the visible FFOV for the LNA optical path is small compared to the fiber NA.

It is a good practice to keep in mind the assumptions of these models. These include constant irradiance of the fiber, and homogeneity of the tissue. Additionally, the models ignore random interference patterns and speckle fields, in relation to the scattering of laser light from weakly ordered media such as tissue<sup>13</sup>. While such effects can contribute to the OCM signal, it is considered noise and it is anticipated that is small enough to be ignored. Also, different absorption mechanisms are ignored since they occur at a much lower probability than elastic scattering by a factor of  $\sim 10^{-6}$ . Finally, while MPM relies on 2PEF and 3PEF, the models assume that the tissue is not fluorescent at the illumination excitation wavelengths, and that no auto-fluorophores are present in the material adding to the expected signals. The application of such phenomena, would require physical models that are complex and computationally prohibitive at current times. Therefore, the illumination and the collection of the MPM signals were modeled separately.

### 3. RESULTS

#### 3.1 Design Tradeoffs

The most important tradeoffs were made during the design phase. Since both HNA and LNA optical paths were using the same optical system, their NAs, FOVs and image quality were dependent of each other. To achieve the desired HNA of  $\sim .40$ , the LNA had to be degraded to a value of  $.016$  instead of the  $.012$  specified for the LNA. The HNA was prioritized to achieve MPM and OCM imaging. The final value for the HNA is  $.42$  exceeding the requirement listed in section 2.1.

Table 2. Final system specifications.

Specification	Desired Value	Value	Note
HNA	.40	.42	Requirement exceeded
HNA full field of view	$100 \mu\text{m}$	$120 \mu\text{m}$	Requirement exceeded
HNA working distance	$.50 \mu\text{m}$ (for contact scanning)	$.50 \mu\text{m}$ (for contact scanning)	Requirement meet
LNA	.012	.016	Requirement unmet
LNA full field of view	$70^\circ$ (desirable)	$30^\circ$	Requirement unmet
LNA working distance	Unconstrained	4-6 mm	-
Diameter	1.5 mm	1.5 mm	Requirement meet
Illumination fiber NA	.12	.12	Requirement meet

Image quality was assessed using the spot diagrams of the system. During optimization of the optical system, it was noted that if the system was optimized for the HNA spot size, the LNA spot will increase and the LNA FFOV will decrease. Since the spot size is imperative for MPM lateral resolution, the HNA spot size was given preference and maintained close to ideal values by sacrificing LNA FFOV and LNA spot size. The potential results of this tradeoff are expected to be seen in the navigation modality of the endoscope. By having a larger LNA spot size, the reconstructed image by the scanning system will have less “effective pixels” for resolution<sup>9</sup>. Additionally, the FFOV of both systems had to be optimized for at least 100  $\mu\text{m}$  FFOV in the HNA optical path; therefore, the LNA FFOV was again given lower priority to achieve this requirement. Final system specifications are listed in Table 2.

### 3.2 Sequential ray trace results

After the system was optimized, the first model tested was the HNA illumination sequential model seen in Figure 9. This model shows the light propagating from the fiber (left) to the tissue that is submerged in water (right).

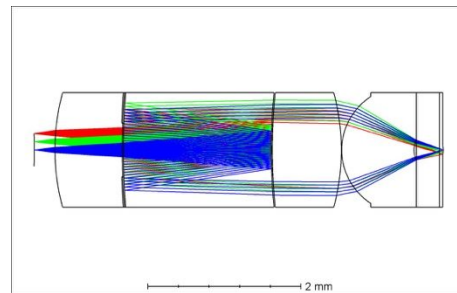


Figure 9. HNA Illumination sequential model.

A collection of plots is shown in Figure 10. Inspecting the Polychromatic Diffraction Merit Transfer Function (MTF), it can be observed that the spatial frequencies from 74 cycles/mm to 592 cycles/mm are severely affected by the obscuration of the telescope light structure. Such degradations, while affecting the resolution of the system in general, are not critical since the system will be reconstructing the image point by point. Also, this can be seen in the optical path difference (OPD) graph. The missing profile at the center, represents the light that reflects directly back to the fiber side and does not make it to the outer dichroic surface. The Seidel plot reveals that the system is mostly aberration free since most of the aberrations were mitigated by introducing negative aberrations in other surfaces. While for some, the Strehl ratio related the Huygens Point Spread Function is not representative of the optical system quality, it is generally accepted that it represents a good measurement of how close to the diffraction limit the system is. The ratio observed in this system is computed as 1.0 when tested by Optics Studio. While the computed Strehl ratio is unlikely, it suggests that the salpingoscope will have a good concentration of energy on each illuminated spot.

Figure 10 also shows the spot sizes of the HNA optical path. The Airy radius obtained by the HNA system is 1.557  $\mu\text{m}$  while the spot sizes across the FOV are  $\leq 1.24 \mu\text{m}$  RMS radius, ensuring that the image will have the expected lateral resolution. Also, the spot size through focus is of importance. The graph suggests that even if the system is not at the right distance, the spot size will be maintained to a relative acceptable size to perform the intended imaging. Note that the spot size through focus shows astigmatism on the off-axis spot diagrams. While astigmatism is the dominant aberration, it is not expected to cause any problems with the imaging modalities.

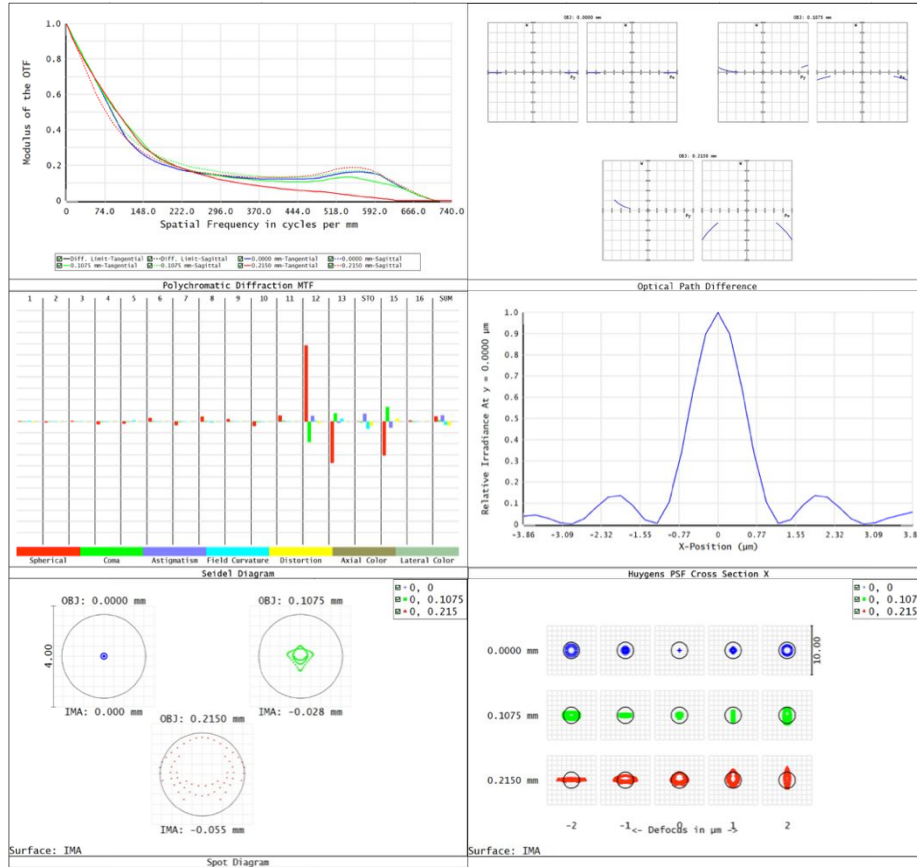


Figure 10. Analysis graphs for the HNA optical path. Graphs shown: MTF (top left), OPD (top right), Seidel diagram (middle left), Huygens PSF (middle right), spot size for 3 fields (bottom left), spot size through focus (bottom right).

The LNA optical path illumination is presented in Figure 11, and its respective collection of plots is presented in Figure 12.

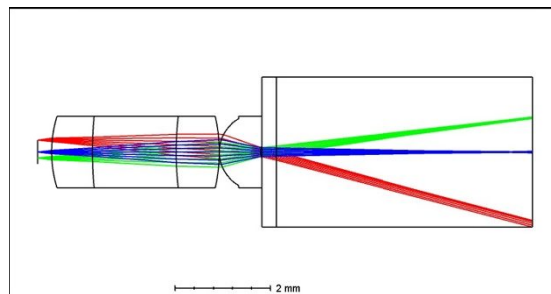


Figure 11. LNA Illumination SEQ model.

In these graphs, it can be observed that several aspects of the LNA system are compromised by the tradeoffs. The MTF is severely degraded at the edge of the FFOV. This is mostly due to the larger spot size that is mostly constant from the exit pupil to infinity. The well-maintained size of spots in a range of about  $\pm 1$  mm serves to maintain resolution in the navigation system. The PSF is also degraded by the larger spot size dispersing energy in a larger area than the diffraction limited airy disk. The OPD and Seidel aberrations are trivial for the LNA system due to the method used for reconstructing the image using a QPT.

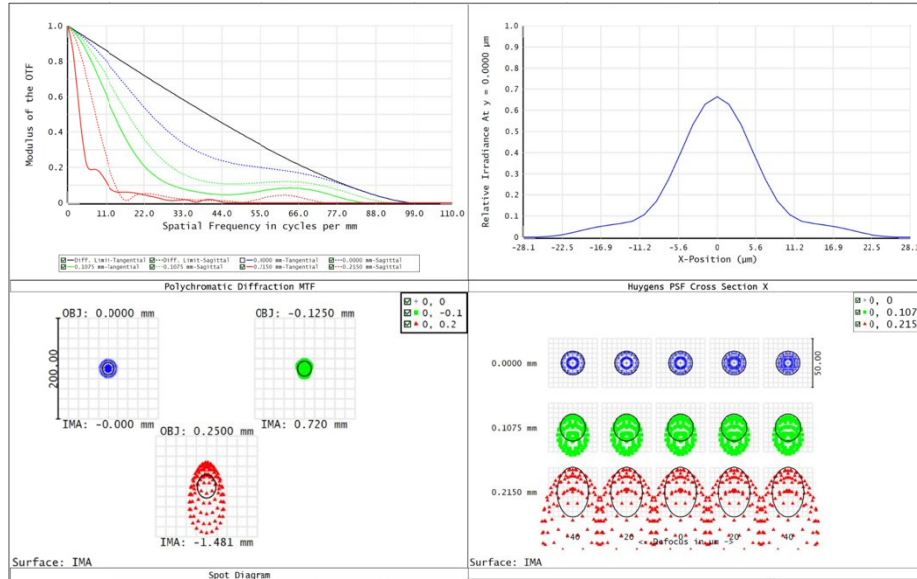


Figure 12. Analysis graphs for the LNA optical path. Graphs shown: MTF (top left), Huygens PSF (top right), spot size for 3 fields (bottom left), spot size through focus (bottom right).

While the LNA optical path is severely degraded, we anticipate that the scanning method will compensate several imaging issues such as the low MTF for most spatial frequencies. By reconstructing point by point of the image, higher spatial frequencies may be computationally resolvable.

### 3.3 Non-Sequential ray trace results

Energy transport efficiencies, light coherence and SMFs collection capability were modeled in non-sequential mode. To evaluate the efficiency of the LNA optical path combined with the collection SMFs, the object modeling the tissue was placed at a distance of 4.75 mm, the illumination fiber was set to illuminate with 520 nm wavelength light, non-sequential ray trace was performed, and the collected power by the detectors inside the SMFs were added and averaged over six runs of the simulation. Figure 13 presents the 3D non-sequential model used. This model suggest that the visible system has an on-axis efficiency of  $E_{SMF-collection} = 1.6E-06 \pm .03E-06$  suggesting that it will collect  $\sim 1.6E-04$  of the total emitted light from the fiber.

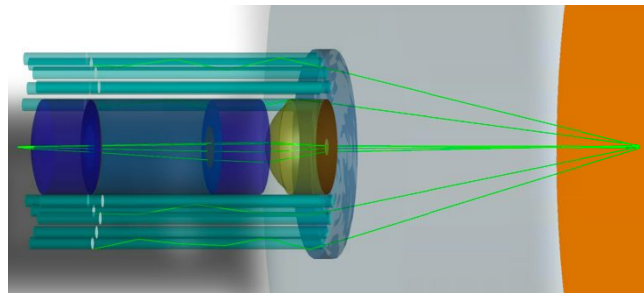


Figure 13. LNA optical path illuminating with 520 nm wavelength and fibers collecting reflected rays from tissue. Only 100 rays were traced for clarity and a filter was applied to show only the rays that reached any of the detectors.

For the MPM and OCM systems, the efficiencies of the illumination system, cladding collection and core collection (Figure 14) are directly related to the dichroic coating profile shown in Figure 4. Note that the efficiencies suggest that the more challenging collection will be the core signal for OCM. This is expected due to the small cross-sectional area available for collection in the fiber core.

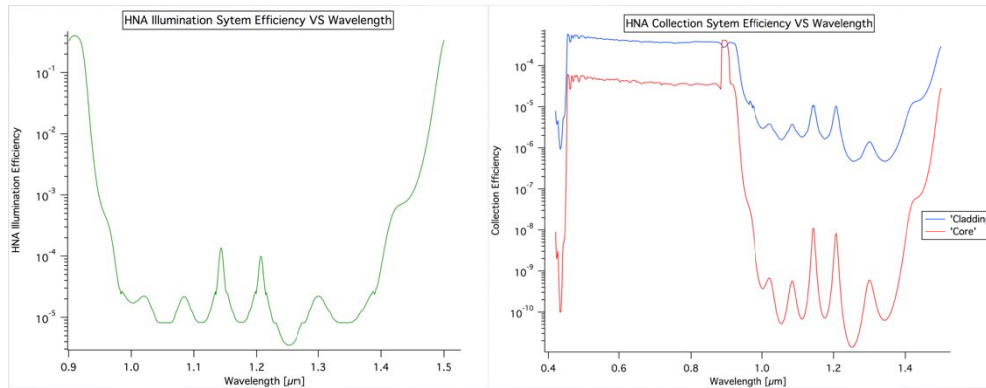


Figure 14. Left, illumination efficiency or energy fraction transported by the optical system at OCM and MPM Illumination wavelengths. Right, collection efficiencies by cladding or core of the scanning fiber indicating the fraction of light collected from the entrance pupil.

To obtain a general idea of the efficiencies of the system, it is necessary to combine the illumination efficiency with the collection efficiencies. Unfortunately, we are unable to model the conversion efficiencies for each of the four MPM signals at this time because multiple parameters must be experimentally determined. The amount of signal generated is dependent of the illumination light characteristics at the tissue such as irradiance, pulse power, pulse duration, repetition rate, and pulse shape in all MPM signals. Although we have specifications for the laser being used in our system, we cannot guarantee what these parameters will hold at the tissue due to dispersion effects of the fiber components and lens system. Each signal also has unique coefficients that would need to be experimentally determined using a sample of ovarian tissue. In the case of 2PEF and 3PEF the respective absorption cross sections and the quantum efficiencies of the processes are currently unknown. SHG is a  $\chi^2$  process with a non-linear coefficient that has been studied in rat tendon collagen at a laser wavelength centered at 880 nm in the past<sup>17</sup> but was determined to be wavelength dependent. As a result, this coefficient would need to be experimentally determined at 1350 nm. THG is a  $\chi^3$  process and the non-linear coefficient in this arrangement would also require experimental data to determine. Therefore, from these MPM models we can only calculate the fractional efficiency that the system can transport from fiber to tissue and from tissue to fibers. In the other hand, the efficiency for OCM and Visible are readily available. For simplicity and assuming that the reflectance model discussed in section 2.4 is correct for the illumination OCM wavelength 1350 nm, the efficiencies should follow these simple relationships:

$$E_{\text{OCM}}(\lambda) = E_{\text{Illumination}}(\lambda) * .065 * E_{\text{Core-collection}}(\lambda) \quad (4)$$

$$E_{\text{visible}}(520\text{nm}) = 1.6 * 10^{-6} = E_{\text{SMF-Collection}} \quad (5)$$

Where  $E_{\text{OCM}}$  is the efficiency of the OCM modality,  $E_{\text{VISIBLE}}$  is the efficiency of the navigation system. Note that  $E_{\text{OCM}}$  is a function of the wavelength and it can be seen in Figure 15.

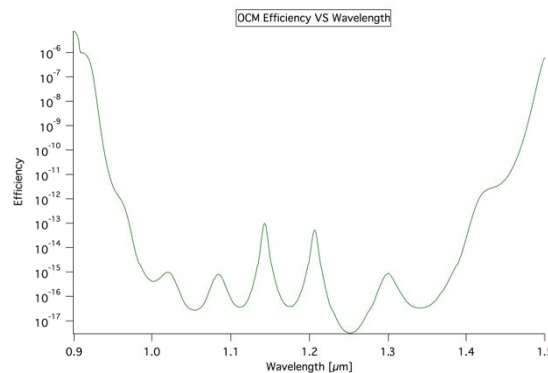


Figure 15.  $E_{\text{OCM}}$  vs Wavelength computed by using Equation 4.

Finally, since OCM needs coherent light, a test to determine the on-axis expected coherent light at the illuminated spot in the tissue was performed. The fiber was set to illuminate at 1350 nm on axis and a detector was placed at the tissue plane. Figure 16 shows the result of this simulation. Note that the coherent irradiance is mostly concentrated in the illuminated spot. While there are coherent rays outside of the illuminated spot, it is anticipated that this additional stray light is not going to be a source of noise due to the spatial separation. The illuminated spot is mostly constant in phase when compared with the rest of the plane. This result increments the level of confidence for OCM functionality.

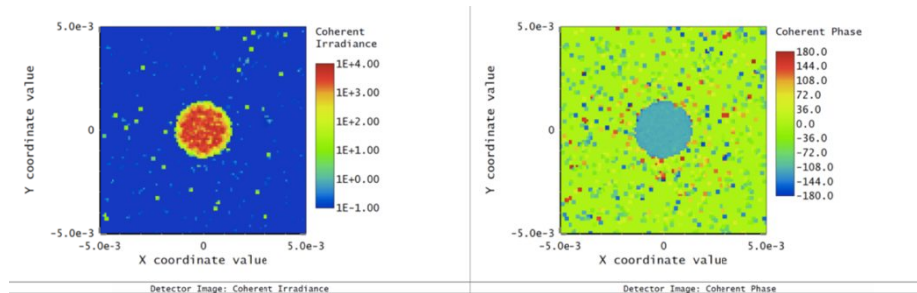


Figure 16. Detector coherent irradiance and phase evaluated at the tissue position for the HNA optical path.

#### 4. FUTURE WORK

The microendoscope presented here is currently under fabrication. Testing and characterization of the assembled endoscopes will be reported and contrasted with the results obtained by the models in future work. Also, evaluation of the system with *ex vivo* ovarian surgical samples will be imaged, analyzed and compared with histology to confirm high sensitivity and specificity for OC. Eventually, the team hopes for human trials to test capability at the point of care.

A signal to noise ratio (SNR) analysis still needs to be completed for the OCM system. Stray light and back reflections may represent a problem for the OCM signal if they are within the coherence length of the laser. The non-sequential ray trace model presented in section 3.3 should provide the necessary information for the SNR evaluation. Unfortunately, Optic Studio does not have laser coherence analysis capability. Therefore, the model requires advanced programming to create a tool that can analyze the ray databases provided by the software.

#### 5. CONCLUSION

While the analysis presented suggest that LNA optical path is degraded off axis, the team is prepared to work around the image degradation using computational methods and in practice the center of the field of view of the navigation system is the most important. Therefore, we do not anticipate any issues with the LNA optical path. Models suggest that the HNA optical path is robust with the exception of its efficiencies. This is due to the materials used in the lenses (David et al. SPIE OSD #10690-32, In preparation). ZnS used in element 2, has a large absorption coefficient which affects both illumination and collection efficiencies.

The salpingoscope presented here has the potential to image the molecular and tissue microstructure changes in ovaries necessary to detect early stage OC, allowing physicians to have an effective screening tool. Compared to laparoscopy and histology, the salpingoscope is less invasive and could be used for regular screening, particularly in high risk women.

#### SUPPORTERS

Research supported in part by the National Institutes of Health (NIH/NIBIB 1R01EB020605) and NSF Graduate Research Fellowship Program (NSF-GRFP).

#### REFERENCES

- [1] American Cancer Society, Inc., "Ovarian Cancer," cancer.org, 18th, December 2017, <<http://www.cancer.org/cancer/ovariancancer/index> > (2nd January 2017).

- [2] Jennifer Kehlet Barton, Babak Amirsolaimani, Photini Rice, Kenneth Hatch, Khanh Kieu, "Three-photon imaging of ovarian cancer," Proc. SPIE 9689, Photonic Therapeutics and Diagnostics XII, 96893P (2016).
- [3] D. Ouzounov, D. R. Rivera, C. M. Brown, W. W. Webb, and C. Xu, "Dual Modality Microendoscope with Optical Zoom Capability," in Conference on Lasers and Electro-Optics 2012, OSA Technical Digest (online) (Optical Society of America, 2012), paper ATTh5A.2.
- [4] Tyler Tate, Molly Keenan, Elizabeth Swan, John Black, Urs Utzinger, Jennifer Barton, "Optical design of an optical coherence tomography and multispectral fluorescence imaging endoscope to detect early stage ovarian cancer," Proc. SPIE 9293, International Optical Design Conference 2014, 92931F (2014);
- [5] K. Kieu, A. Evans, J. Klein, J. Barton, and N. Peyghambarian, "Ultra-high resolution all-reflective OCT system with a compact fiber-based supercontinuum source," in CLEO:2011 - Laser Applications to Photonic Applications, OSA Technical Digest (CD) (Optical Society of America, 2011), paper CWB2.
- [6] K. Kieu, S. Mehravar, R. Gowda, R. A. Norwood, and N. Peyghambarian, "Label-free multi-photon imaging using a compact femtosecond fiber laser mode-locked by carbon nanotube saturable absorber," Biomed. Opt. Express 4, 2187-2195 (2013)
- [7] Fujimoto, James G., Pitris, Costas, Boppart, Stephen A., Brezinski, Mark E., "Optical coherence tomography: An emerging technology for biomedical imaging and optical biopsy," Neoplasia, 2(1-2):9-25 (2000)
- [8] Tsai, P.S. et al. [Principles, design, and construction of a two-photon laser scanning microscope for in vitro and in vivo brain imaging. In *Vivo Optical Imaging of Brain Function*], Frostig, R.D., ed., CRC Press, New York, 2002.
- [9] Lee, C. M., Engelbrecht, C. J., Soper, T. D., Helmchen, F., & Seibel, E. J. "Scanning fiber endoscopy with highly flexible, 1-mm catheterscopes for wide-field, full-color imaging," Journal of Biophotonics, 3(5-6), 385–407. (2010).
- [10] Kelli, Jennifer Kehlet Barton, " Proximal design for a multimodality endoscope with multiphoton microscopy, optical coherence microscopy and visual modalities," Proc. SPIE 10501, 10501-44, (2018).
- [11] W. Drexler, J.G. Fujimoto (eds.), [Optical Coherence Tomography], Springer International Publishing, Switzerland (2015)
- [12] Barbara G. Grant, [Field Guide to Radiometry], SPIE Press, Bellingham, WA (2011).
- [13] Caroline Boudoux, [Fundamentals of Biomedical Optics], Blurb, San Francisco CA (2017)
- [14] Zemax LLC., "Optics Studio Online End User Manual," Zemax.com, January 201, <<http://customers.zemax.com/os/resources/learn/tutorials/online-end-user-manual>> (2nd January 2017).
- [15] J.H. Takano, T. Yakushiji, I. Kamiyama, T. Nomura, A. Katakura, N. Takano, T. Shibahara, "Detecting early oral cancer: narrowband imaging system observation of the oral mucosa microvasculature," International Journal of Oral and Maxillofacial Surgery, Volume 39, Issue 3, (2010) p 208-213.
- [16] Yasumasa Ezoe, Manabu Muto, Noriya Uedo, Hisashi Doyama, Kenshi Yao, Ichiro Oda, Kazuhiro Kaneko, Yoshiro Kawahara, Chizu Yokoi, Yasushi Sugiura, Hideki Ishikawa, Yoji Takeuchi, Yoshibumi Kaneko, Yutaka Saito, "Magnifying Narrowband Imaging Is More Accurate Than Conventional White-Light Imaging in Diagnosis of Gastric Mucosal Cancer", Gastroenterology, Volume 141, Issue 6, (2011), p 2017-2025.e3.
- [17] Theodossiou, T. A., Thrasivoulou, C., Ekwobi, C., & Becker, D. L. "Second Harmonic Generation Confocal Microscopy of Collagen Type I from Rat Tendon Cryosections," Biophysical Journal, 91(12), 4665–4677. (2006)